Journal of
Applied
Crystallography

ISSN 1600-5767

Received 20 January 2014
Accepted 26 February 2014

Crystallographic study of grain refinement of Al by Nb addition

Feng Wang,[a] Dong Qiu,[a] Zhi-Lin Liu,[a] John A. Taylor,[a] Mark A. Easton[b]‡ and Ming-Xing Zhang[a]*

[a]School of Mechanical and Mining Engineering, The University of Queensland, St Lucia, QLD 4072, Australia, and [b]Department of Materials Engineering, Monash University, Clayton, VIC 3800, Australia. Correspondence e-mail: mingxing.zhang@uq.edu.au

The grain refinement of Al by the addition of a small amount of peritectic-forming solute, Nb, has been studied from the crystallographic point of view. Combining the observations of optical microscopy and scanning electron microscopy with the results of energy-dispersive X-ray spectroscopy and X-ray diffraction, it is confirmed that the particles observed at or near the grain centres of refined Al alloys are pro-peritectic Al_3Nb particles. The crystallographic matching between the Al_3Nb particles and Al grains has also been evaluated using an edge-to-edge matching model and further verified using electron backscatter diffraction and transmission electron microscopy. It is found that there are reproducible crystallographic orientation relationships between the Al_3Nb particles and Al grains, and the experimental results are consistent with the predictions of the edge-to-edge matching model. This implies that the pro-peritectic Al_3Nb particles are favourable nucleation sites for Al grains from the crystallographic point of view. Furthermore, the analysis of the size distribution of Al_3Nb particles reveals that the Al_3Nb particles at the grain centres have relatively large particle size, which also corroborates the high potency of Al_3Nb according to the free growth model. It is therefore concluded that the significant grain refinement resulting from the addition of Nb is predominantly attributed to the *in situ* formed Al_3Nb particles which promote grain refinement *via* enhanced heterogeneous nucleation.

1. Introduction

Grain refinement of Al alloys through addition of master alloys, which contain effective grain refiners, is common practice in commercial foundries because it is the most convenient, practical and low cost approach to achieve fine grains. This not only improves the casting soundness and mechanical properties but also increases the formability during subsequent forming processes and ensures consistently better performance of the final products (McCartney, 1989; Murty *et al.*, 2002; Quested, 2004). During the past six decades, extensive research has been carried out to clarify the mechanism underlying grain refinement, and a number of theories/models have been proposed (Cibula, 1949, 1951; Crossley & Mondolfo, 1951; Marcantonio & Mondolfo, 1971; Backerud *et al.*, 1991; Jones & Pearson, 1976; Easton & StJohn, 1999*a*,*b*; Johnsson *et al.*, 1993; StJohn *et al.*, 2011; Greer *et al.*, 2003; Quested & Greer, 2004). It is now well recognized that two essential components, *i.e.* numerous potent nuclei and sufficient effective solutes, are required for effective grain refinement (Easton & StJohn, 1999*a*,*b*; Greer *et al.*, 2003; Johnsson *et al.*, 1993; StJohn *et al.*, 2011). Nevertheless, the details of the mechanism are still in debate as none of the currently existing theories can fully explain all of the phenomena observed in experiments and practice. Central to the major controversial issues is the determination of factors that control the efficiency of grain refinement. Factors such as the contact angle (Turnbull, 1953) and crystallographic matching (Bramfitt, 1970) between nucleant particles and matrix metals/alloys, the geometry and size of nucleant particles (Greer *et al.*, 2000; Qian, 2007), the interactions between nucleant particles and alloy chemistry (Schumacher *et al.*, 1998; Johnsson, 1994*a*,*b*), and the settling of nucleant particles (Jones & Pearson, 1976) have been suggested to affect grain refinement efficiency. Among all these factors, the crystallography between the nucleant particles and matrix and the size of nucleant particles have been considered to be of critical significance in controlling the efficiency of grain refinement.

It is well known that a low-energy interface is favourable to good crystallographic matching with one or more reproducible orientation relationships (ORs) between the nucleant particles and matrix metal. Such an interface facilitates heterogeneous nucleation and hence leads to effective grain

‡ Present address: School of Aerospace, Mechanical and Manufacturing Engineering, RMIT University, Bundoora, VIC 3083, Australia.

refinement (Zhang, Kelly, Easton & Taylor, 2005; Zhang, Kelly, Qian & Taylor, 2005). Conventionally, the crystallographic matching was simply evaluated by the lattice matching (Bramfitt, 1970; Johnsson & Eriksson, 1998; Tondel, 1994), which is calculated from lattice parameters only and thus represents the matching between lattice points rather than real atoms. However, most of the actual nucleant particles have more complicated crystal structures, in which case it is the real atoms that form the interface between phases. To solve this problem, an edge-to-edge matching (E2EM) model (Zhang & Kelly, 2005*a*,*b*), which was developed to examine the actual atomic matching, has thus been employed to evaluate the crystallographic matching between the nucleant phase and metal matrix.

The E2EM model was first proposed by Zhang & Kelly (2005*a*,*b*) to predict possible ORs between any two phases from first principles. The model is based on the assumption that the interfacial crystallographic relationships are governed by the minimization of interfacial strain energy through the matching of parallel atomic rows in the two phases. In order to maximize the atomic matching along the parallel rows, the matching rows should be along close-packed or nearly close-packed directions which have close interatomic spacing. The matching rows can be either straight or zigzag, but the model requires that straight rows match with straight rows while zigzag rows match with zigzag rows. In addition, a pair of close-packed or nearly close-packed planes with similar interplanar spacing is required that contain the matching rows. These planes are termed matching planes. Once the interatomic misfit (f_r) along the matching direction and interplanar mismatch (f_d) between the matching planes are smaller than the critical values (*e.g.* f_r and f_d both <10%) in a given system, an OR between the two phases can potentially form and they can be expressed in terms of the parallelism of the matching rows and near parallelism of the planes. Any small angular deviation between the matching planes and the orientation of the interface plane can be further determined by using the **Δg** criterion (Zhang & Purdy, 1993; Zhang *et al.*, 2000). Using the E2EM model, the relative potency of common grain refiners in both Al and Mg alloys has been successfully evaluated (Zhang, Kelly, Easton & Taylor, 2005; Zhang, Kelly, Qian & Taylor, 2005; Qiu, Zhang, Fu *et al.*, 2007). In addition, the Si-poisoning effect in Al–Si alloys (Qiu, Taylor *et al.*, 2007), the co-poisoning effect of Zr and Ti in Al alloys (Qiu *et al.*, 2010), and the refining effect arising from superheating in Mg alloys (Qiu, Taylor *et al.*, 2007) have also been elucidated by this model. Furthermore, the E2EM model has achieved exciting success in predicting and developing new grain refiners for alloys based on Mg–Y (Qiu *et al.*, 2009) and Mg–Al (Fu *et al.*, 2008).

Recently, the crucial role of the size of inoculant particles in grain refinement and the significant effect of the size distribution of inoculant particles on grain size have been elegantly demonstrated by Greer and co-workers using a free growth model (Greer *et al.*, 2000; Greer & Quested, 2006; Quested & Greer, 2004; Quested & Greer, 2005). The free growth model proposes that the grain initiation is not controlled by the nucleation of a nucleus on an inoculant particle but by the free growth of the nucleus on the particle. A critical undercooling is required for a nucleus on the inoculant particle for the free growth to occur. From the classical expression for the critical nucleus radius at small undercooling, the critical undercooling for free growth, ΔT_{fg}, and the diameter, d, of the inoculant particle are related by $\Delta T_{fg} = 4\sigma/\Delta S_V d$ where σ is the solid–liquid interfacial energy and ΔS_V is the entropy of fusion per unit volume. Based on the free growth model, predictions of as-cast grain size as a function of grain refiner addition level, solute content in the melt and cooling rate have been made. The predictions quantitatively fit the measured grain size in standard (TP-1) tests on commercial purity and other aluminium alloys inoculated with an Al–Ti–B refiner. In addition, Krajewski and Greer (Krajewski, 2006; Krajewski & Greer, 2006) studied the microstructure of cast Zn–25 wt% Al alloy grain refined by a Zn–4 wt% Ti master alloy. They found that many *in situ* formed $L1_2$ Ti(Al, Zn)$_3$ particles with a size of around a few micrometres were located within the refined α'-Zn–Al grains, which agrees well with the free growth model. Furthermore, the mechanisms that control the as-cast grain size in directional solidification have also been determined using this model.

We have recently re-examined the grain refining effect of solutes including Ti, Zr, Nb and V, all of which are peritectic-forming solutes in pure Al (Wang *et al.*, 2013). In order to understand the underlying mechanism of grain refinement through addition of these solutes, the grain size was plotted against the inverse value of the growth restriction factor, $1/Q$, to clarify the grain refinement obtained. It appeared that the considerable grain refinement obtained by the addition of Nb is likely to be due to the *in situ* formation of pro-peritectic Al_3Nb particles that act as nucleant particles to promote heterogeneous nucleation. However, details that support this hypothesis have yet to be provided. The aim of the present work is to provide comprehensive experimental evidence to verify the proposition made previously. Therefore, in this article, the identity of the nucleant particles will be first determined by scanning electron microscopy (SEM) and X-ray diffraction (XRD). Following that, the crystallographic matching between the nucleant phase and Al matrix will be evaluated using the E2EM model. The prediction will then be experimentally verified by electron backscatter diffraction (EBSD) and transmission electron microscopy (TEM). In addition, the size distributions of both the active nucleant particles at grain centres and the dormant nucleant particles along grain boundaries will also be measured through the image analysis of SEM micrographs. This will then be analysed using the free growth model.

2. Experimental

Al alloys with different Nb addition levels (0, 0.12, 0.2 and 0.5%) were prepared by adding compact Al–Nb pellets into high-purity commercial Al melt followed by casting. The chemical compositions of pure Al and Al–Nb alloys were analysed by inductively coupled plasma atomic emission

Table 1
Chemical compositions of pure Al and Al–Nb alloys (wt%).

Sample	Al	Nb	Si	Fe	Ti	B	C
Pure Al	Balance	0.01	0.016	0.017	0.002	0.0001	0.0001
Al–0.12Nb	Balance	0.10	0.021	0.025	0.002	0.0002	0.001
Al–0.2Nb	Balance	0.18	0.015	0.023	0.003	0.0002	0.002
Al–0.5Nb	Balance	0.43	0.028	0.034	0.002	0.0001	0.004

spectroscopy and the values measured are listed in Table 1. All compositions throughout the article are given as weight percent unless otherwise specified. The pellets were made by mixing pure Nb powder with Al chips followed by compression of the mixture in a die. All Al melts were prepared in clay-bonded graphite crucibles, which were placed in a resistance furnace and heated to 953 K. After adding the compact pellets, the melt was isothermally held at 953 K for 20 min and stirred immediately before dipping preheated graphite moulds in the melt to collect samples. The sample melt was then placed in between two pieces of insulating board and cooled to ambient temperature in air. Details of the casting procedure have been described previously (Wang *et al.*, 2013).

Metallographic samples were transversely sectioned approximately 10 mm from the base of the small cast ingots and were mechanically ground and polished. These samples were firstly examined under an optical microscope with polarized light after anodizing using a 0.5% HBF_4 solution for approximately 2 min at 20 V. The grain sizes were measured using a linear intercept technique (ASTM E112-10). Phases were identified through XRD using a Bruker D8 diffractometer, and micrographs were further obtained using scanning electron microscopy with a JEOL-6460LA electron microscope. XRD was performed at 40 kV with Cu $K\alpha$ radiation (wavelengths $\lambda_{K\alpha1}$ = 1.54056 Å). Crystallographic orientation relationships between the observed nucleant particles and the Al grains were determined using an automated EBSD facility equipped with an orientation imaging system in SEM.

A focused ion beam (FIB) technique was used to prepare the TEM foils because a site-specific sample is required. The positions of the intermetallic particles sitting at the grain centres were firstly located using the SEM mode in the FIB and then the particles were cut out together with the Al matrix. A typical preparation process for TEM foils through the FIB/SEM approach is illustrated in Fig. 1. The TEM foils, with a thickness of around 80–90 nm, were then examined in a JEOL 2100 transmission electron microscope operated at 200 kV.

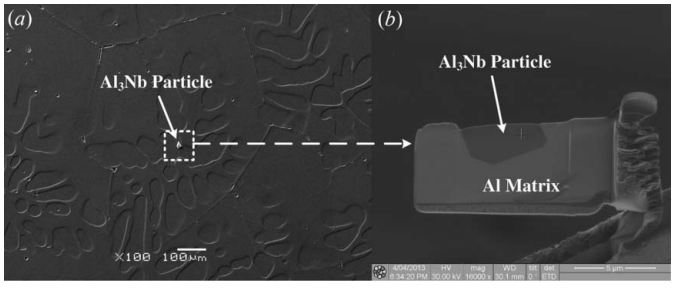

Figure 1
(*a*) Typical SEM image of an Al_3Nb particle sitting at an Al grain centre; (*b*) FIB image of an Al_3Nb particle embedded in the Al matrix, which was cut out from the grain centre in (*a*).

3. Results and discussion

3.1. Optical microstructure of Al–Nb alloys

The typical as-cast microstructure of Al alloys with different additions of Nb is shown in Fig. 2. Columnar structure is observed and the grain size remains almost unchanged when the addition of Nb is below 0.12%. However, at 0.2% Nb addition, there is an evident microstructure transition from columnar to equiaxed grains and a reduction in grain size from approximately 1000 µm (Figs. 2*a* and 2*b*) to about 600 µm (Fig. 2*c*). With further addition of Nb to 0.5% Nb, the grain size slightly decreases to around 500 µm as shown in Fig. 2(*d*).

In order to identify the factors that are responsible for the grain refinement, the as-cast Al alloys were firstly examined using XRD to ascertain the change of phase constituents with Nb addition level. The XRD spectra are shown in Fig. 3. It is found that the peaks in Figs. 3(*a*) and 3(*b*) are all from the α-Al phase, indicating that these two alloys (pure Al and Al–0.12% Nb) contain no other phases but α-Al. In contrast, extra peaks other than those from the α-Al phase are reproducibly observed in Figs. 3(*c*) and 3(*d*). A comparison of the 2θ angles of the extra peaks with the Powder Diffraction File database (2002 PCPDF-WIN V. 2.3) reveals that these extra peaks are the reflections of the Al_3Nb phase. This agrees well with the equilibrium Al–Nb phase diagram (Elliott & Shunk, 1981), indicating that an Al_3Nb phase has indeed formed during the solidification process in the Al alloys with additions of 0.2 and 0.5% Nb.

The same samples were then further examined using SEM to characterize the microstructure details of the Al alloys with different Nb contents. It is found that, in the alloys with fine equiaxed grains (*i.e.* Al–0.2% Nb and Al–0.5% Nb), inter-

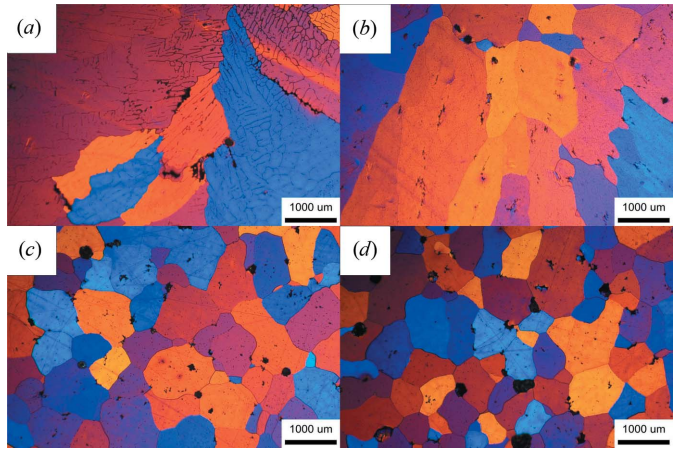

Figure 2
Typical micrographs of as-cast Al alloys with different Nb addition levels: (*a*) pure Al, *d* = 1103 µm; (*b*) 0.12% Nb, *d* = 1032 µm; (*c*) 0.2% Nb, *d* = 642 µm and (*d*) 0.5% Nb, *d* = 482 µm.

metallic particles are observed at or near the grain centres as shown in Fig. 4(*a*). However, no trace of such intermetallic particles can be detected in the alloy samples with coarse columnar structure, *i.e.* Al–0.12% Nb, as shown in Fig. 4(*b*). A typical energy-dispersive X-ray (EDX) spectrum on the particles observed at or near the grain centres is shown in Fig. 4(*c*). An analysis of the spectrum reveals that these particles are enriched with Al and Nb and that the atomic ratio of Al to Nb is approximately 3:1, which is consistent with that of the Al_3Nb phase.

Combining the XRD, SEM and optical microstructure observations, it is reasonable to conclude that the pronounced grain refinement is only achieved in the alloys containing more than 0.2% Nb. In these alloys, there is a distinct presence of Al_3Nb particles at or near grain centres. In terms of the Al–Nb phase diagram, such Al_3Nb particles are the pro-peritectic phase. The question arises as to whether these particles can act as the nucleation sites to facilitate the grain refinement of Al alloys.

3.2. Crystallography of Al_3Nb and α-Al in Al–Nb alloys

In order to clarify the potency of the pro-peritectic Al_3Nb particles as nucleants for Al, the crystallography between Al_3Nb and Al has been studied using the E2EM model. In general, the crystallographic evaluation based on the E2EM model includes two major steps: (1) identification of the close-packed atomic rows and close-packed planes in terms of the crystal structure and atomic positions of both phases, and (2) calculation of the interatomic spacing misfit (f_r) along the matching rows and the interplanar spacing mismatch (f_d) between the matching planes. Al possesses a face-centred cubic (f.c.c.) structure with lattice parameter a = 0.4049 nm (Villars & Calvert, 1991) and it has one close-packed straight row along the $\langle 101\rangle^{S}_{Al}$ direction and one nearly close-packed zigzag row along the $\langle 211\rangle^{Z}_{Al}$ direction; the superscripts 'S' and 'Z' are used to distinguish straight and zigzag rows. As a simple f.c.c. structure, Al has three close-packed or nearly close-packed planes. The most close-packed plane is $\{111\}_{Al}$ which contains both $\langle 101\rangle^{S}_{Al}$ and $\langle 211\rangle^{Z}_{Al}$ directions. $\{020\}_{Al}$ is the second most close-packed plane but it only contains the $\langle 101\rangle^{S}_{Al}$ direction. The third most close-packed plane is $\{220\}_{Al}$ and it also contains both $\langle 101\rangle^{S}_{Al}$ and $\langle 211\rangle^{Z}_{Al}$ directions. The atomic configuration of Al within the most close-packed plane, (111), is shown in Fig. 5(*a*).

Al_3Nb has a tetragonal crystal structure with lattice parameters a = 0.3841 and c = 0.8609 nm. Each unit cell contains six Al atoms and two Nb atoms (Villars & Calvert, 1991). The most close-packed plane of Al_3Nb is {112}, which contains four close-packed or nearly close-packed rows: $\langle 421\rangle^{Z}_{Al_3Nb}$, $\langle 111\rangle^{Z}_{Al_3Nb}$, $\langle 110\rangle^{S}_{Al_3Nb}$ and $\langle 021\rangle^{S}_{Al_3Nb}$. The second most close-packed plane is the {004} plane, which contains only one close-packed row, $\langle 110\rangle^{S}_{Al_3Nb}$. Another possible close-packed plane of the Al_3Nb crystal is the {020} plane which also contains one close-packed row, $\langle 021\rangle^{S}_{Al_3Nb}$. The atomic configuration of Al_3Nb within its most close-packed plane (112), together with the close-packed directions on it, is shown in Fig. 5(*b*).

In terms of the identified close-packed rows and close-packed planes, the values of interatomic misfit, f_r, and interplanar mismatch, f_d, between Al and Al_3Nb are calculated. The results are illustrated in Fig. 6. As we can see from Fig. 6(*a*), all the values of f_r along the close-packed rows between Al and Al_3Nb are less than 6%. It is worth mentioning that, according to the E2EM model, the straight rows are required to match with straight rows and the zigzag rows match with zigzag rows. However, as shown in Fig. 6(*b*),

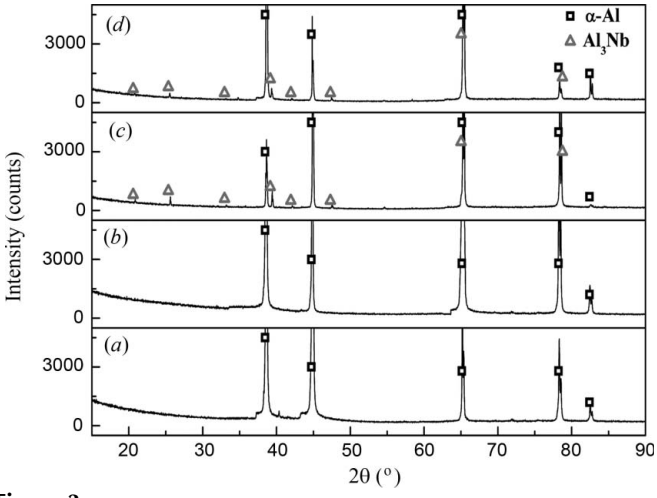

Figure 3
XRD spectra of the as-cast Al alloys: (*a*) pure Al, (*b*) 0.12% Nb, (*c*) 0.2% Nb and (*d*) 0.5% Nb.

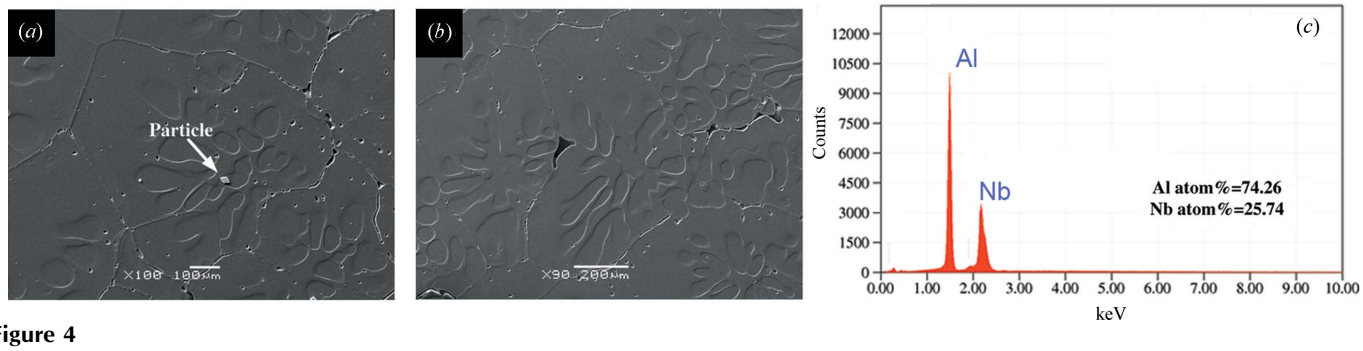

Figure 4
(*a*) SEM secondary electron image showing a typical Al_3Nb particle at the centre of a grain in an Al alloy with the addition of 0.2% Nb, (*b*) SEM secondary electron image showing no presence of Al_3Nb particles in the Al alloy with the addition of 0.12% Nb and (*c*) EDX spectrum taken from the particle at the grain centre in (*a*).

there are only four pairs of close-packed planes between Al and Al_3Nb that have an interplanar mismatch, f_d, below 10%. They are $\{111\}_{Al} \parallel \{112\}Al_3Nb$ with f_d = 1.78%, $\{111\}Al \parallel \{004\}Al_3Nb$ with f_d = 8.63%, $\{020\}Al \parallel \{004\}Al_3Nb$ with f_d = 5.93% and $\{020\}Al \parallel \{020\}Al_3Nb$ with f_d = 5.43%.

According to the E2EM model, to form an OR, matching rows must lie in matching planes. The close-packed row pairs with f_r less than 10% and the corresponding close-packed plane pairs that contain these row pairs with f_d less than 10% are represented in Fig. 7. Occasionally, a given pair of rows may lie in more than one pair of close-packed planes. Therefore, the arrows are used to indicate the associated plane pairs for a given row pair.

Combining the matching row pairs with the associated matching plane pairs that carry the matching rows, six possible ORs can be formulated, as listed in Table 2.

Using the **Δg** parallelism criterion (Zhang & Purdy, 1993; Zhang *et al.*, 2000), these six possible ORs can be further refined. Refinement of the OR (1) gives the OR (I) in Table 3, whereas no solution to the refinement of the OR (2) can be obtained. After refinement, the OR (3) can be more accurately expressed as the OR (II) in terms of the $[110]_{Al_3Nb}$ and $[02\bar{1}]_{Al_3Nb}$ directions and the $(\bar{1}12)_{Al_3Nb}$ plane for consistency in Table 3. Refining the ORs (4), (5) and (6) gives the same OR and it is listed as the OR (III) in Table 3. Therefore, three distinguishable ORs between Al and Al_3Nb are finally predicted.

Table 2
Rough crystallographic ORs between Al and Al_3Nb predicted using the E2EM model.

ORs	Nearly parallel direction	Nearly parallel plane
OR (1)	$\langle 101\rangle^{S}_{Al} \parallel \langle 02\bar{1}\rangle^{S}_{Al_3Nb}$	$\{111\}_{Al} \parallel \{112\}_{Al_3Nb}$
OR (2)	$\langle \bar{2}11\rangle^{Z}_{Al} \parallel \langle 11\bar{1}\rangle^{Z}_{Al_3Nb}$	$\{111\}_{Al} \parallel \{112\}_{Al_3Nb}$
OR (3)	$\langle \bar{2}11\rangle^{Z}_{Al} \parallel \langle \bar{4}21\rangle^{Z}_{Al_3Nb}$	$\{111\}_{Al} \parallel \{112\}_{Al_3Nb}$
OR (4)	$\langle 101\rangle^{S}_{Al} \parallel \langle 110\rangle^{S}_{Al_3Nb}$	$\{111\}_{Al} \parallel \{112\}_{Al_3Nb}$
OR (5)	$\langle 101\rangle^{S}_{Al} \parallel \langle 110\rangle^{S}_{Al_3Nb}$	$\{020\}_{Al} \parallel \{004\}_{Al_3Nb}$
OR (6)	$\langle 101\rangle^{S}_{Al} \parallel \langle 110\rangle^{S}_{Al_3Nb}$	$\{111\}_{Al} \parallel \{004\}_{Al_3Nb}$

To experimentally verify the prediction of the E2EM model, ORs between the Al_3Nb particles at or near grain centres and the associated Al grains were determined using automated EBSD. The EBSD patterns from both the Al_3Nb particles and the related Al grains were recorded and indexed based on the corresponding lattice parameters. Fig. 8(*a*) shows a typical SEM image where an Al_3Nb particle is clearly observed near

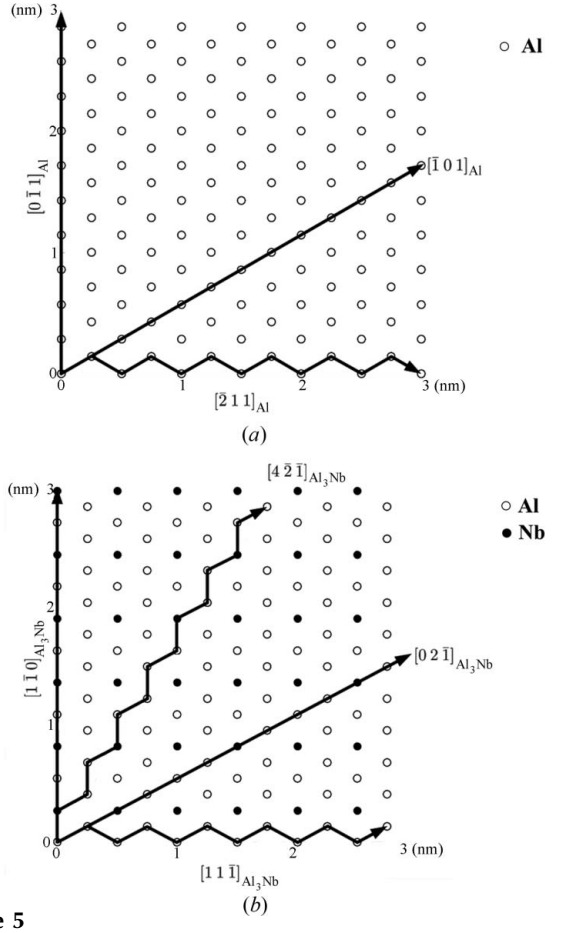

Figure 5
Atomic configurations of Al and Al_3Nb on their respective most close-packed planes: (*a*) $(111)_{Al}$ and (*b*) $(112)_{Al_3Nb}$. The bold lines highlight the close-packed rows within these planes.

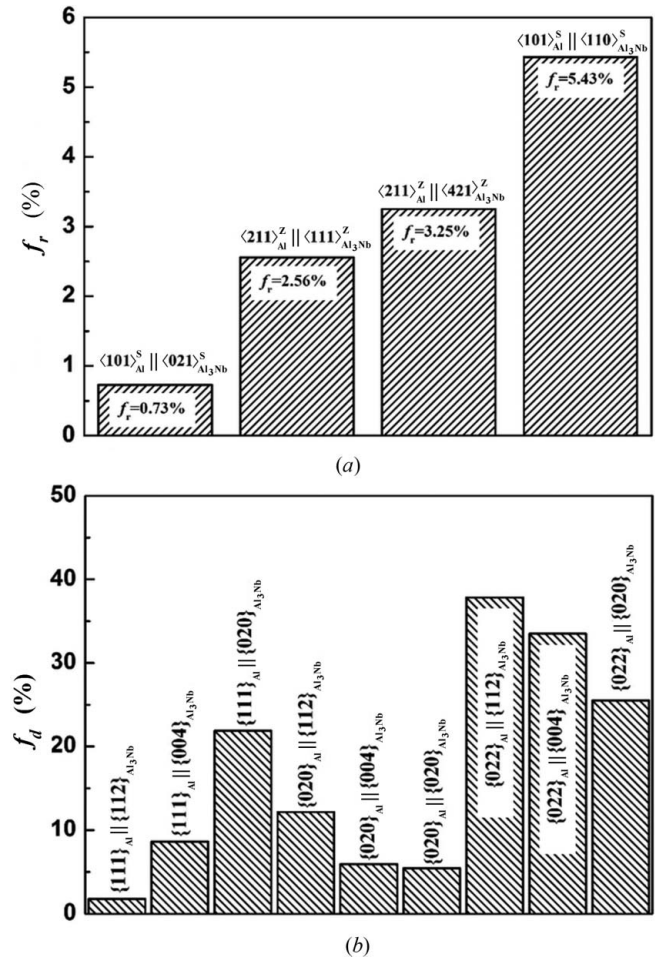

Figure 6
(*a*) Interatomic spacing misfit, f_r, along the close-packed rows and (*b*) interplanar spacing mismatch, f_d, between the close-packed and nearly close-packed planes of Al and Al_3Nb.

Table 3
Final crystallographic ORs between Al and Al_3Nb predicted using the E2EM model and the **Δg** parallelism criterion.

ORs	Nearly parallel directions (1)	Nearly parallel directions (2)	Nearly parallel plane
OR (I)	$[0\bar{1}1]^S_{Al}$ 2.13° from $[110]^S_{Al_3Nb}$	$[101]^S_{Al} \parallel [02\bar{1}]^S_{Al_3Nb}$	$(\bar{1}11)_{Al}$ 1.07° from $(\bar{1}12)_{Al_3Nb}$
OR (II)	$[0\bar{1}1]^S_{Al}$ 1.85° from $[110]^S_{Al_3Nb}$	$[101]^S_{Al}$ 1.64° from $[02\bar{1}]^S_{Al_3Nb}$	$(\bar{1}11)_{Al}$ 1.76° from $(\bar{1}12)_{Al_3Nb}$
OR (III)	$[0\bar{1}1]^S_{Al} \parallel [110]^S_{Al_3Nb}$	$[101]^S_{Al}$ 1.92° from $[02\bar{1}]^S_{Al_3Nb}$	$(\bar{1}11)_{Al}$ 0.24° from $(\bar{1}12)_{Al_3Nb}$

the grain centre. The corresponding EBSD patterns taken from the Al_3Nb particle and from the Al grain are shown in Figs. 8(*b*) and 8(*c*), respectively. It can be seen that the $[110]_{Al_3Nb}$ pole in the EBSD pattern of the Al_3Nb particle is very close to the $[0\bar{1}1]_{Al}$ pole in the EBSD pattern of the Al grain, while the $[02\bar{1}]_{Al_3Nb}$ pole is also very close to the $[101]_{Al}$ pole. In addition, the $(\bar{1}12)_{Al_3Nb}$ band is almost parallel to the $(\bar{1}11)_{Al}$ band. Therefore, the OR shown in Fig. 8 can be roughly expressed as $[110]_{Al_3Nb} \parallel [0\bar{1}1]_{Al}$, $[02\bar{1}]_{Al_3Nb} \parallel [101]_{Al}$, $(\bar{1}12)_{Al_3Nb} \parallel (\bar{1}11)_{Al}$.

To accurately and reliably determine the ORs using the EBSD technique, a large number of Al_3Nb particle and Al grain pairs need to be examined. To improve the efficiency and accuracy of examination, a simple numerical approach based on Euler angles (Qiu *et al.*, 2009) was employed to determine the ORs. In the present work, the Euler angles of 25 pairs of Al_3Nb particles and the related Al grains were recorded. The experimentally determined ORs are expressed in a stereographic projection in terms of the $[001]_{Al}$ direction and $(001)_{Al}$ plane, as shown in Fig. 9. For comparison, the predictions from the E2EM model are also expressed in the stereographic projection. Two directions, $[110]_{Al_3Nb}$ and $[02\bar{1}]_{Al_3Nb}$, and one plane, $(\bar{1}12)_{Al_3Nb}$, are selected to express the ORs in terms of the Al crystal structure. It is worth noting that, since the stereographic projections of direction and plane poles for the f.c.c. crystal structure are identical, all the direction and plane poles in this article are therefore expressed in one stereographic projection (Fig. 9) for the sake of brevity.

As shown in Fig. 9(*a*), the experimental ORs agree reasonably well with the ORs predicted by the E2EM model, which corroborates the evaluation of the E2EM model. A closer inspection of all the ORs on a larger scale, as illustrated in Figs. 9(*b*), 9(*c*) and 9(*d*), reveals that the experimental ORs scatter about the three predicted ORs with no tendency to group around a particular predicted OR. This is either the real case or probably an experiment error due to the accuracy limitation of the EBSD technique.

In an attempt to increase the accuracy of the experimental ORs, the ORs between the Al_3Nb particles and Al grains were further determined using convergent-beam Kikuchi line diffraction patterns (CBKLDP) in TEM. A typical TEM image of an overall view of an Al_3Nb particle embedded in the Al matrix and the corresponding Kikuchi line diffraction patterns from the Al_3Nb particle and the Al matrix are shown in Fig. 10. After indexing the Kikuchi line diffraction patterns, the OR between the Al_3Nb and Al can be calculated using the method developed by Zhang & Kelly (1998*a*,*b*): it is $[110]_{Al_3Nb}$ 0.62° from $[0\bar{1}1]_{Al}$, $[02\bar{1}]_{Al_3Nb}$ 1.58° from $[101]_{Al}$ and $(\bar{1}12)_{Al_3Nb}$ 0.68° from $[1\bar{1}\bar{1}]_{Al}$.

Using the TEM–CBKLDP approach, ten pairs of Al_3Nb particles and Al

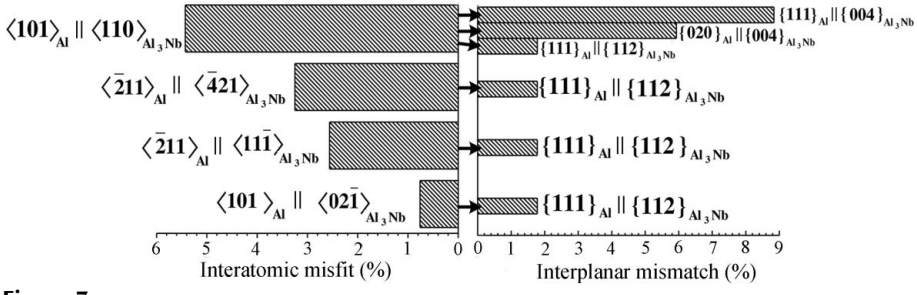

Figure 7
Graphic representation of the matching row pairs and the related suitable matching plane pairs that contain the matching row pairs as predicted by the E2EM model.

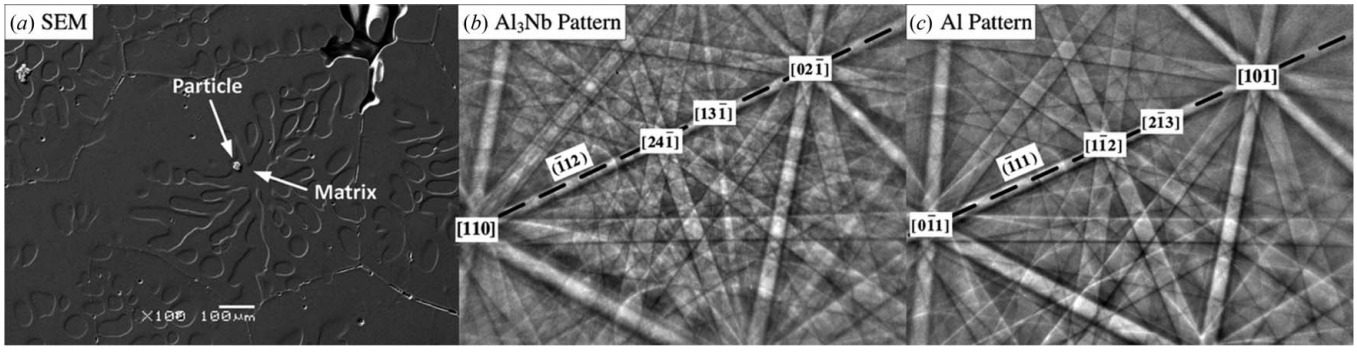

Figure 8
(*a*) A typical SEM micrograph showing an Al_3Nb particle near the centre of an Al grain, (*b*) the corresponding EBSD pattern from the Al_3Nb particle and (*c*) the associated EBSD pattern from the Al grain.

grains were examined. It is found that six of them show reproducible ORs, while the other four pairs exhibit completely random ORs. The particles exhibiting random ORs are unlikely to have acted as nucleants for Al grains during solidification. For comparison, the six reproducible ORs are also expressed in the stereographic projection as shown in Fig. 9. It can be seen that the ORs determined using TEM through the CBKLDP approach are generally consistent with those determined using the EBSD approach and with those predicted by the E2EM model. This further verifies the evaluation of the E2EM model and hence validates the favourable crystallographic matching between Al_3Nb and Al. However, contrary to expectation, the accuracy of the experimentally determined ORs using the TEM–CBKLDP approach has not much improved compared to those determined using the EBSD approach, because the results are also scattered. This is probably attributable to bending of the TEM foils, which was created during the final FIB milling/thinning process as a result of their own weight. This bending would cause the variation of the respective crystallographic orientations of the Al_3Nb particle and Al matrix, and therefore affect the determined OR.

In addition, it is interesting to mention that, in the Al–0.5% Nb alloy, multiple Al_3Nb particles were occasionally observed at or near the grain centres, as shown in Fig. 11. The EBSD and TEM study on these particles indicated that only one of these particles exhibits an OR consistent with those predicted by the E2EM model while the other particles exhibit random ORs. This implies that only the particle exhibiting the OR consistent with an Al grain acted as nucleant. Other particles just happened to be trapped at the grain centre during solidification. In addition, a number of Al_3Nb clusters were also observed along the grain boundaries, and the size of the cluster increases with the addition level. This indicates that, as the content of Nb is increased to 0.5 wt%, the *in situ* formed Al_3Nb particles show increasing tendency to agglomeration, which has been considered to adversely affect the ductility of castings because these clusters of brittle Al_3Nb particles may initiate cracks and defects. This is especially important in the production

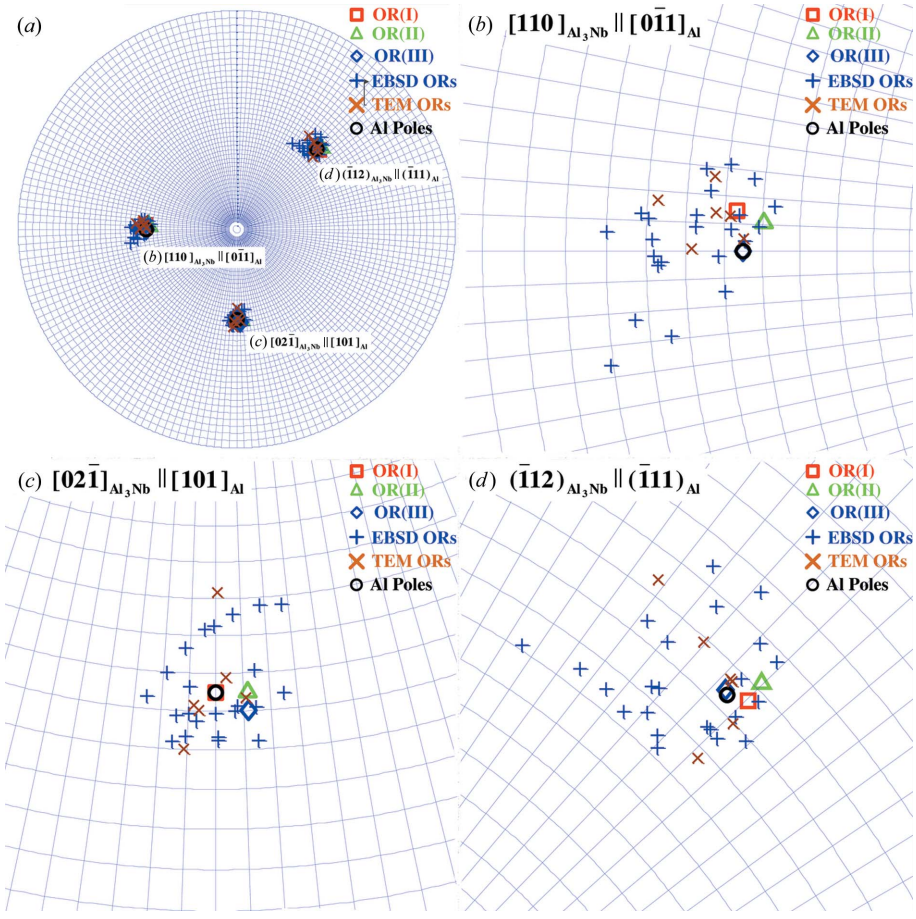

Figure 9
Stereographic projection showing the experimental and predicted ORs between Al_3Nb particles and Al grains, plotted in terms of f.c.c. Al in the [001] direction.

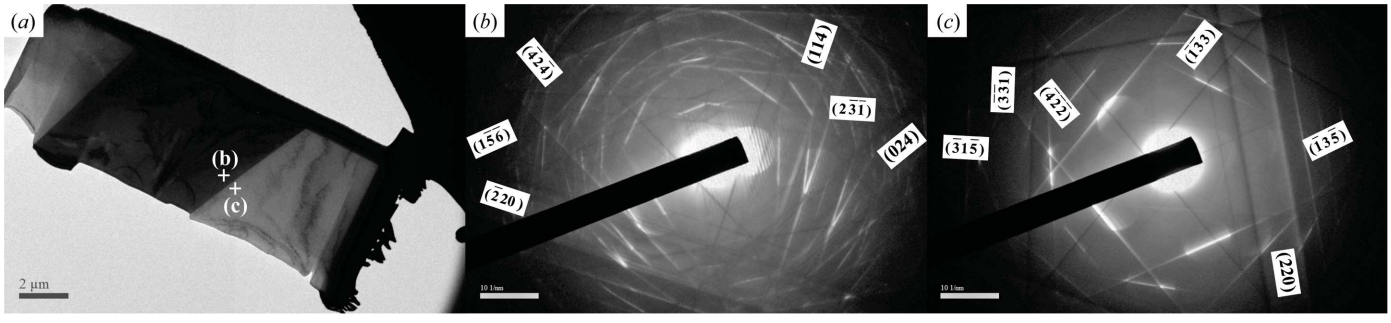

Figure 10
(*a*) Typical TEM micrograph showing an Al_3Nb particle embedded in the Al matrix, (*b*) Kikuchi line diffraction pattern from the Al_3Nb particle and (*c*) Kikuchi line diffraction pattern from the Al matrix.

Table 4
Interatomic spacing misfit (%) and interplanar spacing mismatch (%) between the Al matrix and different nucleant particles calculated in terms of the E2EM model (Zhang & Kelly, 2005*a*).

Nucleant phase	f_r along matching rows		f_d between matching planes	
Al_3Nb	$[02\bar{1}]_{Al_3Nb} \parallel [101]_{Al}$ 0.73	$[110]_{Al_3Nb} \parallel [0\bar{1}1]_{Al}$ 5.43	$(\bar{1}12)_{Al_3Nb} \parallel (\bar{1}11)_{Al}$ 1.78	$(020)_{Al_3Nb} \parallel (020)_{Al}$ 5.43
Al_3Ti	$[02\bar{1}]_{Al_3Ti} \parallel [1\bar{1}0]_{Al}$ 0.7	$[\bar{1}10]_{Al_3Ti} \parallel [1\bar{1}0]_{Al}$ 5.0	$(112)_{Al_3Ti} \parallel (111)_{Al}$ 1.6	$(200)_{Al_3Ti} \parallel (200)_{Al}$ 5.0
TiC	$[001]_{TiC} \parallel [001]_{Al}$ 6.9	$[011]_{TiC} \parallel [011]_{Al}$ 6.9	$(200)_{TiC} \parallel (200)_{Al}$ 6.4	$(200)_{TiC} \parallel (111)_{Al}$ 7.4
TiB_2	$[1\bar{2}10]_{TiB_2} \parallel [011]_{Al}$ 6.1	$[1\bar{1}00]_{TiB_2} \parallel [\bar{1}\bar{1}2]_{Al}$ 6.1	$(10\bar{1}1)_{TiB_2} \parallel (200)_{Al}$ 0.9	$(11\bar{2}0)_{TiB_2} \parallel (\bar{2}20)_{Al}$ 6.1
AlB_2	$[1\bar{2}10]_{AlB_2} \parallel [011]_{Al}$ 5.1	$[1\bar{1}00]_{AlB_2} \parallel [\bar{1}\bar{1}2]_{Al}$ 5.1	$(10\bar{1}1)_{TiB_2} \parallel (200)_{Al}$ 0.6	$(11\bar{2}0)_{TiB_2} \parallel (\bar{2}20)_{Al}$ 5.1

of thin aluminium foil. Therefore, from a practical point of view, it is necessary to carefully control the Nb addition to limit surplus Nb content and hence minimize agglomeration when manufacturing Al–Al_3Nb master alloys.

Previous studies (Zhang, Kelly, Easton & Taylor, 2005; Zhang, Kelly, Qian & Taylor, 2005; Qiu *et al.*, 2010; Qiu, Taylor *et al.*, 2007; Qiu, Zhang, Fu *et al.*, 2007; Qiu, Zhang, Taylor *et al.*, 2007; Qiu *et al.*, 2009; Fu *et al.*, 2008) on grain refinement in terms of the E2EM model have demonstrated that the grain refining efficiency of a grain refiner depends on the values of f_r and f_d. Smaller interatomic misfit and interplanar mismatch correspond to higher grain refining efficiency due to the lower interfacial energy between the grain refiner and the solid formed on the refiner. Table 4 lists the values of f_r and f_d between Al and different nucleant particles including some commercial grain refiners for Al (Zhang, Kelly, Easton & Taylor, 2005). It should be mentioned that Al_3Nb has an isomorphous structure with Al_3Ti. It is noticed that the values of f_r and f_d between Al and Al_3Nb are very small and are close to those between Al and Al_3Ti. Furthermore, the OR between Al and Al_3Nb determined in the present article is very similar to the ORs between Al and Al_3Ti published by Arnberg *et al.* (1982) (A-B-K), who reported their OR as follows: $(011)_{Al_3Ti} \parallel (012)_{Al}$, $[010]_{Al_3Ti} \parallel [010]_{Al}$ or $(001)_{Al_3Ti} \parallel (010)_{Al}$, $[010]_{Al_3Ti} \parallel [010]_{Al}$. It should be mentioned that the above expressions of OR are incorrect because the directions do not lie in the associated planes. Instead, the A-B-K OR can be re-expressed as follows: $(011)_{Al_3Ti} \parallel (012)_{Al}$, $[100]_{Al_3Ti} \parallel [100]_{Al}$ or $(001)_{Al_3Ti} \parallel (100)_{Al}$, $[100]_{Al_3Ti} \parallel [001]_{Al}$. By using Euler's theorem, the difference between the present OR between Al and Al_3Nb and the A-B-K OR between Al and Al_3Ti has been evaluated. The calculation indicates that these two ORs are related by a rotation of 1.04° about an axis that is very close to $[100]_{Al}$. The above crystallographic analysis implies that Al_3Nb should have a similar grain refining potency to Al_3Ti from the crystallographic point of view. However, the actual grain refining efficiency of Al_3Nb is lower than that of Al_3Ti. This is probably because of the low growth restriction factor of Nb in Al (~1 K) (Wang *et al.*, 2013) compared with the extremely high value of the growth restriction factor of Ti in Al (~10 K for normal Ti additions) (Easton & John, 2001; Wang *et al.*, 2013).

3.3. Effect of the nucleant particle size and size distribution on grain refinement

As mentioned above, the size of nucleant particles also plays an important role in grain refinement, which can be evaluated well by the free growth model (Greer *et al.*, 2000; Greer & Quested, 2006; Quested & Greer, 2004, 2005). Therefore, the size distributions of the total Al_3Nb particles (including particles at or near grain centres and along grain boundaries) and of the active Al_3Nb particles at or near grain centres were measured and the results are shown in Fig. 12. It should be mentioned that, strictly speaking, the size of the nucleation substrate in the free growth model refers to the size of major facets of the polygonal Al_3Nb particles exposed to the liquid Al. This would involve the determination of the exact major crystal facets where the Al grains nucleate and the accurate measurement of size of the major facets in real three-dimensional morphology. In the current article, alternatively, the equivalent diameter of a circle which has the same area as the actual cross section of Al_3Nb particles as shown in a two-dimensional SEM image was used as a rough approximation of the size of the nucleation substrate. The size distributions of the total Al_3Nb particles in the Al–0.2% Nb and Al–0.5% Nb alloys are within the range from 0 to 50 µm. This is much broader than the normal size distribution of TiB_2 particles (0–6 µm) observed in the commercial grain refiners used in Al alloys (Greer *et al.*, 2000; Quested & Greer, 2004). The significantly large size of Al_3Nb is considered to be a result of the slow cooling

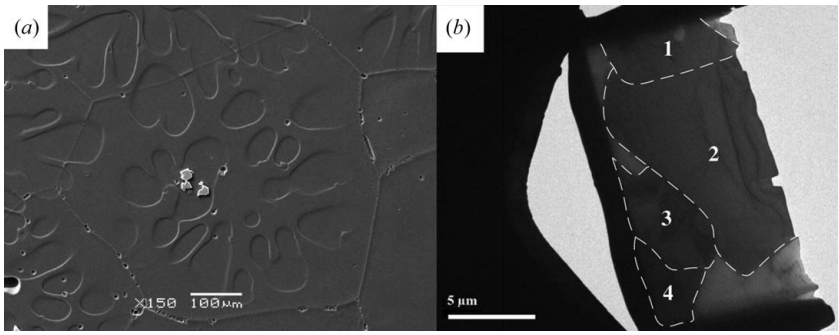

Figure 11
(*a*) SEM image showing three Al_3Nb particles near the grain centre and (*b*) TEM overall view showing four Al_3Nb particles embedded in the Al matrix which were cut out from near the grain centre.

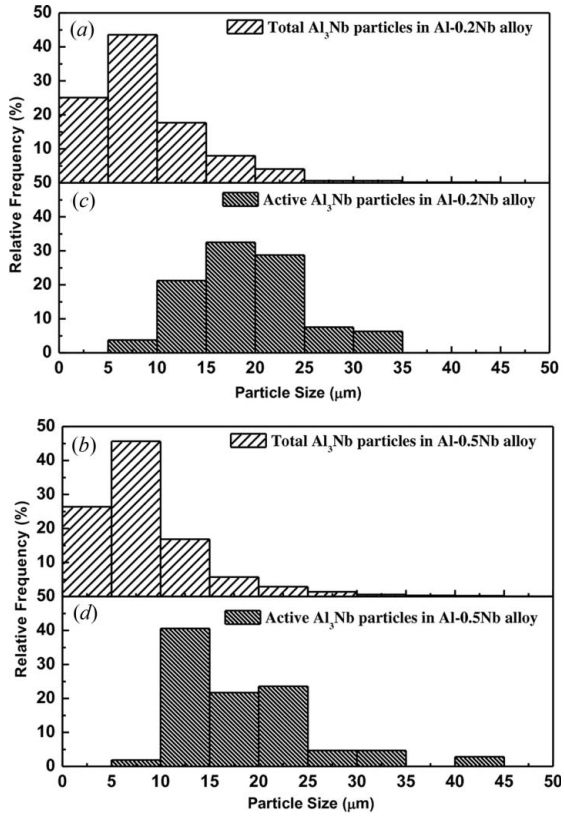

Figure 12
Size distributions of the total Al_3Nb particles at grain centres and along grain boundaries in (*a*) the Al–0.2 wt% Nb alloy and (*b*) the Al–0.5 wt% Nb alloy and the size distributions of the active Al_3Nb particles at grain centres in (*c*) the Al–0.2 wt% Nb alloy and (*d*) the Al–0.5 wt% Nb alloy.

(1 K s^{-1}) used in the present casting experiment, which allows more time for the pro-peritectic Al_3Nb particles to grow during the solidification. According to the free growth model, bigger nucleant particles require less undercooling to activate the heterogeneous nucleation on them. Therefore, the large size of the Al_3Nb particles further confirms the high potency of Al_3Nb as a nucleant for Al. Further examination of the size distributions of the total Al_3Nb particles reveals that the majority (approximately 70%) of the total Al_3Nb particles are smaller than 10 μm. In contrast, most (more than 95%) of the active nucleant particles at grain centres are larger than 10 μm, which lies at the upper end of the size distributions of the total Al_3Nb particles as illustrated in Fig. 12. This is consistent with the free growth model, which proposes that larger particles become active first as the temperature is lowered and smaller nucleant particles remain inactive if the maximum undercooling reached in the melt does not exceed their critical undercooling, ΔT_{fg} (Greer *et al.*, 2000; Greer & Quested, 2006; Quested & Greer, 2004, 2005).

Combining the favourable crystallographic matching between the Al_3Nb particles and Al grains with the large size of Al_3Nb particles, it is substantiated that the *in situ* formed pro-peritectic Al_3Nb particles in the Al–Nb alloys are powerful nucleant particles for Al. This validates the hypothesis that the considerable grain refinement achieved by the addition of Nb is mainly attributable to the Al_3Nb particles, which promote grain refinement *via* enhanced heterogeneous nucleation.

4. Conclusions

The E2EM model predicts three orientation relationships between the pro-peritectic Al_3Nb and Al in Al–Nb alloys. They are experimentally verified using both EBSD and TEM–CBKLDP approaches. These ORs are as follows:

OR (I): $[110]^{S}_{Al_3Nb}$ 2.13° from $[0\bar{1}1]^{S}_{Al}$, $[02\bar{1}]^{S}_{Al_3Nb} \parallel [101]^{S}_{Al}$, $(\bar{1}12)_{Al_3Nb}$ 1.07° from $(\bar{1}11)_{Al}$;

OR (II): $[110]^{S}_{Al_3Nb}$ 1.85° from $[0\bar{1}1]^{S}_{Al}$, $[02\bar{1}]^{S}_{Al_3Nb}$ 1.64° from $[101]^{S}_{Al}$, $(\bar{1}12)_{Al_3Nb}$ 1.76° from $(\bar{1}11)_{Al}$;

OR (III): $[110]^{S}_{Al_3Nb} \parallel [0\bar{1}1]^{S}_{Al}$, $[02\bar{1}]^{S}_{Al_3Nb}$ 1.92° from $[101]^{S}_{Al}$, $(\bar{1}12)_{Al_3Nb}$ 0.24° from $(\bar{1}11)_{Al}$.

The present work substantiates that the significant grain refinement obtained through the addition of Nb is primarily attributed to the *in situ* formed pro-peritectic Al_3Nb particles, which facilitate heterogeneous nucleation as these particles have both an excellent crystallographic matching with Al and a large particle size.

The authors are very grateful to the Australian Research Council for funding support. FW would also like to acknowledge the support of the China Scholarship Council. The authors are indebted to Dr Hui Diao at the Queensland University of Technology for training in the FIB technique for TEM sample preparation. The authors acknowledge the facilities, and the scientific and technical assistance, of the Australian Microscopy and Microanalysis Research Facility at the Centre for Microscopy and Microanalysis, The University of Queensland.

References

Arnberg, L., Backerud, L. & Klang, H. (1982). *Metals Technol.* **9**, 7–13.
Backerud, L., Johnsson, M. & Gustafson, P. (1991). *Aluminium*, **67**, 910–915.
Bramfitt, B. (1970). *Metall. Trans.* **1**, 1987–1995.
Cibula, A. (1949). *J. Inst. Met.* **76**, 321–360.
Cibula, A. (1951). *J. Inst. Met.* **80**, 1–16.
Crossley, F. A. & Mondolfo, L. F. (1951). *Trans. Am. Inst. Min. Metall. Pet. Eng.* **191**, 1143–1148.
Easton, M. A. & StJohn, D. H. (1999*a*). *Metall. Mater. Trans. A*, **30**, 1613–1623.
Easton, M. A. & StJohn, D. H. (1999*b*). *Metall. Mater. Trans. A*, **30**, 1625–1633.
Easton, M. A. & StJohn, D. H. (2001). *Acta Mater.* **49**, 1867–1878.
Elliott, R. P. & Shunk, F. A. (1981). *Bull. Alloy Phase Diagrams*, **2**, 75–81.
Fu, H. M., Qiu, D., Zhang, M. X., Wang, H., Kelly, P. M. & Taylor, J. A. (2008). *J. Alloys Compd.* **456**, 390–394.
Greer, A. L., Bunn, A. M., Tronche, A., Evans, P. V. & Bristow, D. J. (2000). *Acta Mater.* **48**, 2823–2835.
Greer, A. L., Cooper, P. S., Meredith, M. W., Schneider, W., Schumacher, P., Spittle, J. A. & Tronche, A. (2003). *Adv. Eng. Mater.* **5**, 81–91.
Greer, A. L. & Quested, T. E. (2006). *Philos. Mag.* **86**, 3665–3680.
Johnsson, M. (1994*a*). *Z. Metallkd.* **85**, 781–785.
Johnsson, M. (1994*b*). *Z. Metallkd.* **85**, 786–789.

Johnsson, M., Backerud, L. & Sigworth, G. K. (1993). *Metall. Mater. Trans. A*, **24**, 481–491.
Johnsson, M. & Eriksson, L. (1998). *Z. Metallkd.* **89**, 478–480.
Jones, G. P. & Pearson, J. (1976). *Metall. Trans. B*, **7**, 223–234.
Krajewski, W. K. (2006). *Mater. Sci. Forum*, **508**, 615–619.
Krajewski, W. K. & Greer, A. L. (2006). *Mater. Sci. Forum*, **508**, 281–286.
Marcantonio, J. A. & Mondolfo, L. F. (1971). *Metall. Trans.* **2**, 465–471.
McCartney, D. G. (1989). *Int. Mater. Rev.* **34**, 247–260.
Murty, B. S., Kori, S. A. & Chakraborty, M. (2002). *Int. Mater. Rev.* **47**, 3–29.
Qian, M. (2007). *Acta Mater.* **55**, 943–953.
Qiu, D., Taylor, J. A. & Zhang, M. X. (2010). *Metall. Mater. Trans. A*, **41**, 3412–3421.
Qiu, D., Taylor, J. A., Zhang, M. X. & Kelly, P. M. (2007). *Acta Mater.* **55**, 1447–1456.
Qiu, D., Zhang, M. X., Fu, H. M., Kelly, P. M. & Taylor, J. A. (2007). *Philos. Mag. Lett.* **87**, 505–514.
Qiu, D., Zhang, M.-X. & Kelly, P. M. (2009). *Scr. Mater.* **61**, 312–315.
Qiu, D., Zhang, M. X., Taylor, J. A., Fu, H. M. & Kelly, P. M. (2007). *Acta Mater.* **55**, 1863–1871.
Qiu, D., Zhang, M. X., Taylor, J. A. & Kelly, P. M. (2009). *Acta Mater.* **57**, 3052–3059.
Quested, T. E. (2004). *Mater. Sci. Technol.* **20**, 1357–1369.
Quested, T. E. & Greer, A. L. (2004). *Acta Mater.* **52**, 3859–3868.
Quested, T. E. & Greer, A. L. (2005). *Acta Mater.* **53**, 4643–4653.
Schumacher, P., Greer, A. L., Worth, J., Evans, P. V., Kearns, M. A., Fisher, P. & Green, A. H. (1998). *Mater. Sci. Technol.* **14**, 394–404.
StJohn, D. H., Qian, M., Easton, M. A. & Cao, P. (2011). *Acta Mater.* **59**, 4907–4921.
Tondel, P. A. (1994). PhD thesis, University of Trondheim, Norway.
Turnbull, D. (1953). *Acta Metall.* **1**, 8–14.
Villars, P. & Calvert, L. D. (1991). *Pearson's Handbook of Crystallographic Data for Intermetallic Phases*, 2nd ed. Materials Park: ASM International.
Wang, F., Liu, Z., Qiu, D., Taylor, J. A., Easton, M. A. & Zhang, M.-X. (2013). *Acta Mater.* **61**, 360–370.
Zhang, M. X. & Kelly, P. M. (1998*a*). *Acta Mater.* **46**, 4081–4091.
Zhang, M. X. & Kelly, P. M. (1998*b*). *Acta Mater.* **46**, 4617–4628.
Zhang, M. X. & Kelly, P. M. (2005*a*). *Acta Mater.* **53**, 1073–1084.
Zhang, M. X. & Kelly, P. M. (2005*b*). *Acta Mater.* **53**, 1085–1096.
Zhang, M. X., Kelly, P. M., Easton, M. A. & Taylor, J. A. (2005*a*). *Acta Mater.* **53**, 1427–1438.
Zhang, M. X., Kelly, P. M., Qian, M. & Taylor, J. A. (2005*b*). *Acta Mater.* **53**, 3261–3270.
Zhang, W. Z. & Purdy, G. R. (1993). *Philos. Mag. A*, **68**, 279–290.
Zhang, W. Z., Ye, F., Zhang, C., Qi, Y. & Fang, H. S. (2000). *Acta Mater.* **48**, 2209–2219.